Design and analysis of high-temperature operating 795 nm VCSELs for chip-scale atomic clocks

2013 Laser Phys. Lett. 10 045802

(http://iopscience.iop.org/1612-202X/10/4/045802)

Laser Phys. Lett. **10** (2013) 045802 (6pp) doi:10.1088/1612-2011/10/4/045802

LETTER

Design and analysis of high-temperature operating 795 nm VCSELs for chip-scale atomic clocks

Jian Zhang[1,2], Yongqiang Ning[1,3], Yugang Zeng[1], Jianwei Zhang[1,2], Jinlong Zhang[1], Xihong Fu[1], Cunzhu Tong[1] and Lijun Wang[1,3]

[1] State Key Laboratory of Luminescence and Application, Changchun Institute of Optics, Fine Mechanics and Physics, Changchun 130033, People's Republic of China
[2] University of Chinese Academy of Sciences, Beijing 100039, People's Republic of China

E-mail: ningyq@ciomp.ac.cn and wanglj@ciomp.ac.cn

Received 22 June 2012, in final form 9 December 2012
Accepted for publication 9 December 2012
Published 8 February 2013
Online at stacks.iop.org/LPL/10/045802

Abstract
We propose a new structure design and analysis of high-temperature (>350 K) operating 795 nm vertical-cavity surface-emitting lasers (VCSELs) for ^{87}Rb based chip-scale atomic clocks (CSACs). Compositions and thicknesses of the InAlGaAs/AlGaAs multiple quantum wells (MQWs) are optimized for high optical gain at elevated temperatures. The temperature sensitivity of the threshold current is estimated by calculating the temperature dependence of the cavity-mode gain. A self-consistent VCSEL model based on quasi-3D finite element analysis is employed to investigate the temperature distribution and output of the proposed structure. An output of 1 mW with a 3 dB bandwidth of 6 GHz is obtained from a 3 μm aperture VCSEL under 2.4 mA current at temperature higher than 340 K. These findings indicate that high-gain QWs and gain-offset consideration are especially crucial to make high-performance VCSELs at elevated temperatures.

(Some figures may appear in colour only in the online journal)

1. Introduction

Vertical-cavity surface-emitting lasers (VCSELs) are attractive for various applications because of their low threshold current [1, 2], high direct modulation speed [3], and low divergence angle of the output beam [4, 5]. In the last few years, due to the other advantages of VCSELs, such as intrinsic spectral stability, low power consumption, and ease of current modulation with RF signals, advances have been made in creating the so-called VCSEL based chip-scale atomic clocks (CSACs) [6], utilizing the spectroscopic technique of coherent population trapping (CPT) [7].

The main challenge of making special VCSELs for CSACs is to improve the high-temperature performance, because the devices must be designed to operate at the same temperatures at which the alkali atom vapor is specified to work [8]. Generally, VCSEL performance is severely degraded at high temperatures, with the threshold current increasing and the slope efficiency decreasing [9]. The modulation speed of VCSELs is also affected by the intrinsic damping of the resonant carrier–photon interaction [10]. In addition, high temperature accelerates VCSEL aging by a factor of two for every 10 °C increase [11].

Much effort has been expanded to improve the temperature characteristics of VCSELs used for optical communication in earlier studies [12–14]. Single-mode

[3] Authors to whom any correspondence should be addressed.

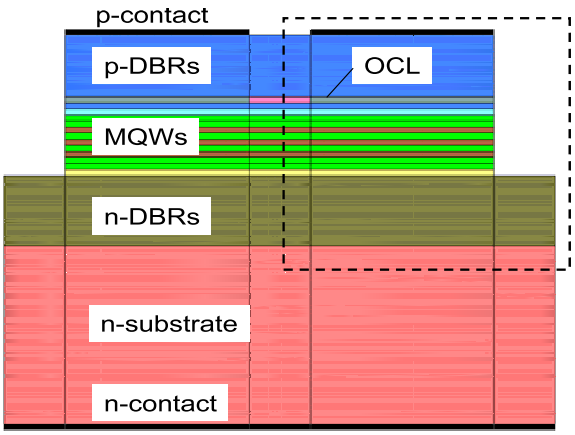

Figure 1. Schematic cross-section of the calculated oxide-confined top-emitting 795 nm VCSEL.

operation [15] and optical modulating characteristics [16] of 795 nm VCSELs based on the AlGaAs active region have been reported. However, quantitative analysis and detailed optimization of high-temperature operating 795 nm VCSELs have not been reported in the literature.

In this study, we propose high-temperature (>350 K) operating 795 nm VCSELs for ^{87}Rb based CSACs with prospective threshold current of 0.9 mA, output of 1 mW and 3 dB bandwidth of 6 GHz. Firstly, compositions and thicknesses in the compressively strained InAlGaAs QW active region are theoretically studied by comparing the band structures and gain-carrier characteristics at high temperatures. Secondly, we evaluate and analyze the temperature sensitivity of the threshold current by comparing the temperature-shift of the cavity mode and the gain-peak wavelength from 300 K to 430 K. Finally, a self-consistent VCSEL model based on quasi-3D finite element analysis is employed to investigate the temperature distribution, temperature-dependent power, and modulation response of the proposed structure.

2. Structure and physical model

2.1. Top-emitting VCSEL structure

The device structure of a 795 nm VCSEL is illustrated in figure 1. The active region consists of three InAlGaAs–AlGaAs QWs sandwiched in two separate confinement heterojunction (SCH) layers to accomplish the 1λ-thick optical cavity. The QWs are placed at the peak position of the standing wave to supply the maximum optical gain. The oxide-confined layer (OCL) is formed by 30 nm $Al_{0.98}Ga_{0.02}As$ adjacent to the top SCH layer. The distributed Bragg reflectors (DBRs) are 32 p-type and 40.5 n-type layer pairs of $Al_{0.25}Ga_{0.75}As/Al_{0.9}Ga_{0.1}As$. The interface layer in each pair is 20 nm with composition grading from 0.25 to 0.9.

2.2. Band structure and optical gain

Model-solid theory [17, 18] is used to calculate the band discontinuity of strained InAlGaAs QWs. The $k\cdot p$ theory with valence band mixing effects is employed to calculate quantum well subbands, following the formulas of Chuang [19] that involve solving a 6 × 6 Hamiltonian of the Luttinger–Kohn type and imposing an envelope function approximation. In the case of valence mixing, the valence bands are not parabolic and the gain spectrum can be expressed in numerical integration over the in-plane wavevector k_t [20]:

$$g(E) = \frac{g_0}{2\pi tE}\sum_{i,j}\int_0^{\infty}\frac{\left(\frac{\pi}{\Gamma}\right)f_{\mathrm{dip}}(k_t)M_b(f_j-f_i)\mathrm{d}k_t^2}{1+(E_{cj}(k_t)-E_{kpi}(k_t)-E)^2/\Gamma^2}. \tag{1}$$

2.3. Basic VCSEL model

A self-consistent VCSEL model combining simulation of carrier transport, self-heating and optical wave-guiding and their close interaction is provided by the Photonic Integrated Circuit Simulator in 3D (PICS3D) software. The carrier transport is described based on the classic drift–diffusion model [20]. The reflection characteristics of DBRs and the longitudinal optical confinement factor are calculated and optimized using a one-dimensional transfer matrix method [21]. Basic parameters used in the simulation are taken from [22].

2.4. Self-heating model and temperature-dependent parameters

Both the ambient temperature rise and the self-heating degrade the VCSEL performance. In VCSELs with small oxide apertures, the self-heating problem becomes more severe due to several factors: the enhanced power density in small device volume, severe Joule heating in DBR stacks, and the oxides that act as electrical and thermal blocking layers.

We quantitatively investigate the aggravated self-heating in oxide-confined 795 nm VCSELs with ambient temperature increasing from 300 to 358 K using PICS3D. All important heat sources, i.e. non-radiative recombination and absorption of spontaneous radiation, are taken into account in the self-heating model, in which conservation of energy requires that the temperature satisfies the heat flux equation

$$\rho_L C_L\frac{\partial T}{\partial t} = -\nabla\cdot\vec{J}_{\mathrm{heat}} + H_{\mathrm{heat}} \tag{2}$$

where ρ_L is the material density and H_{heat} is the heat power density generated by various sources.

In the practical device, the main thermal parameters are temperature dependent refractive index, bandgap (E_g), thermal conductivity (K_L) and specific heat (C_L). The temperature-dependent E_g, K_L and C_L of the binary alloys are calculated by equations (3)–(5) with coefficients from [22]:

$$E_g(T) = E_g(0\ \mathrm{K}) - \frac{\alpha\Theta}{2}\left[\sqrt[p]{1+\left(\frac{2T}{\Theta}\right)^p}-1\right] \tag{3}$$

$$C_L(T) = C_L(300\ \mathrm{K})\frac{20-(\Theta_D/T)^2}{20-(\Theta_D/300\ \mathrm{K})^2} \tag{4}$$

$$\kappa_L(T) = \kappa_L(300\ \mathrm{K})\left(\frac{T}{300\ \mathrm{K}}\right)^{\delta}. \tag{5}$$

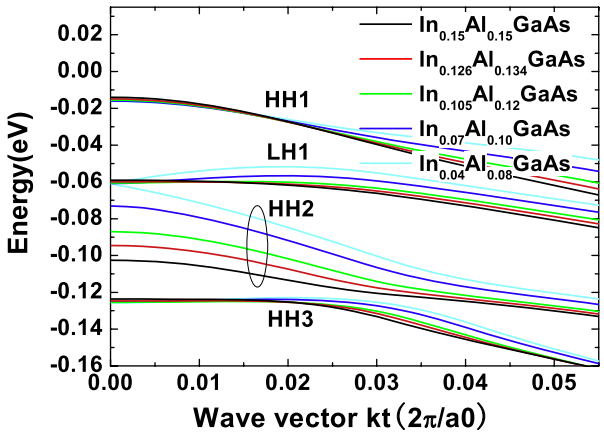

Figure 2. The valence subband structures of InGaAlAs QWs with In composition from 4% to 15%, fixed thickness of 6 nm and barriers of $Al_{0.3}Ga_{0.7}As$. (HH1, the first heavy hole subband; LH1, the first light hole subband; HH2, the second heavy hole subband; HH3, the third heavy hole subband.)

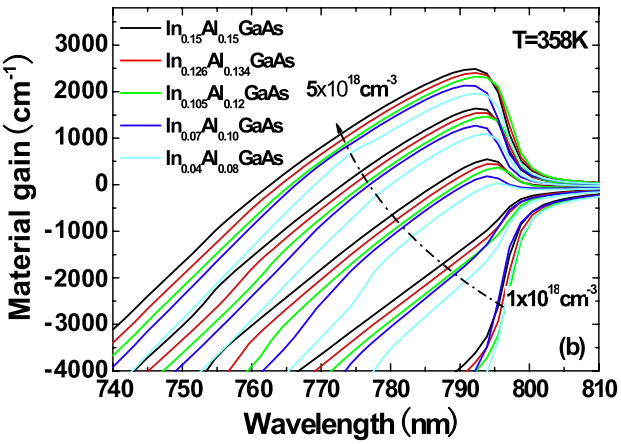

Figure 3. The optical gain spectra of the InAlGaAs QWs with indium compositions from 4% to 15%, carrier densities from 1×10^{18} to 5×10^{18} cm^{-3}, a fixed thickness of 6 nm and barriers of $Al_{0.3}Ga_{0.7}As$ at 358 K.

2.5. Modulation response

The AM and FM modulation response of the VCSEL is analyzed by the small signal dynamic model of PICS3D [23]. We assume the relative response of the photon density to external modulation is the same everywhere and the VCSEL under small external perturbation is operating in a single transverse mode. The mode amplitude then can be made by Taylor expansion of Green's function solution [24] in terms of frequency, carrier and photon density.

3. Results and discussion

3.1. Gain-carrier characteristics of InAlGaAs QWs

InAlGaAs/AlGaAs QWs have been widely employed for lasers emitting at about 0.8 μm and demonstrated superior gain characteristics with respect to unstrained GaAs/AlGaAs QWs [18, 25–27]. Therefore, we choose three InAlGaAs QWs separated by $Al_{0.3}GaAs$ barriers to form the active region of the 795 nm VCSEL structure in figure 1.

The compositions and thicknesses of the QWs are adjusted to optimize the gain characteristics in the following paragraphs while keeping the gain peak at 795 nm. The calculated valence subbands of the series of InAlGaAs QWs with variant indium and aluminum compositions are plotted as a function of the in-plane wavevector k_t in figure 2. As the compressive strain increasing with more indium in the QWs, the strain pushes the HH2 subband away from the LH1 to a higher energy level, resulting in a lower density of states in the valence band. Meanwhile, the curvature of HH1 increases with increasing indium composition, which makes the density of states in the valence and conduction bands better matched. These effects are expected to result in much higher differential gain and lower transparency carrier density.

The optical gain of InAlGaAs/AlGaAs QWs at 358 K with increasing carrier density is depicted in figure 3.

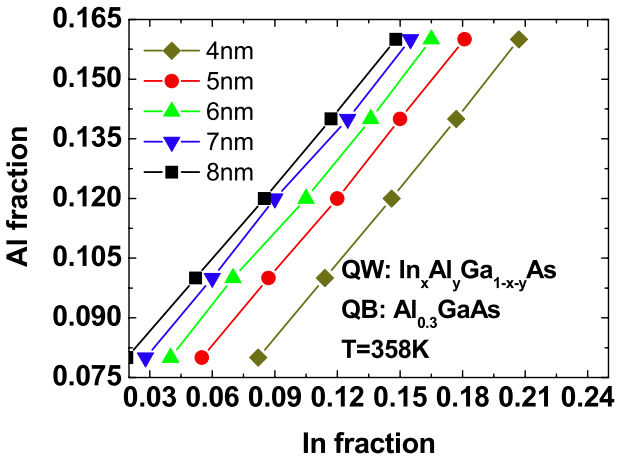

Figure 4. InAlGaAs QWs designed to provide a gain peak at 795 nm at 358 K with variant indium and aluminum compositions, variant thicknesses and fixed barriers of $Al_{0.3}Ga_{0.7}As$.

The material gain increases with indium composition (compressive strain) and tends to saturate when the indium composition is higher than 10%. Furthermore, it is also shown that the spectra keep a broad gain band around the peak wavelength, which is beneficial for VCSELs operating at high temperature.

To optimize the QW thickness, we calculated gain characteristics of InAlGaAs QWs with different thicknesses at 358 K, which is depicted in figure 4. When increasing the QW thickness for improving differential gain, In and Al compositions have to be adjusted to maintain the gain peak at 795 nm. Figure 5 depicts the peak material gain of the InAlGaAs QWs with thickness from 4 to 8 nm as a function of carrier density at 358 K. When the QW thickness increases from 4 to 6 nm (with In composition increasing), the transparency carrier density obviously decreases. This is attributed to the reduced density of valence states, which results in smaller joint densities of states. However, when the QW thickness increases further from 6 to 8 nm, the

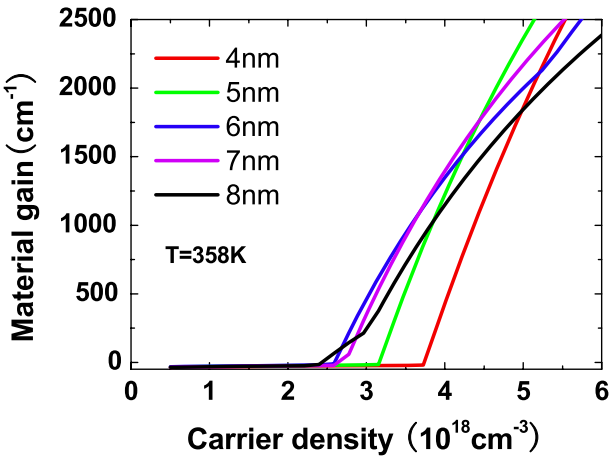

Figure 5. The peak gain of the InAlGaAs QWs as a function of carrier density at 358 K. The QW thickness varies from 4 to 8 nm with In and Al compositions adjusted to ensure the gain peak is located at 795 nm. The barriers are 6 nm $Al_{0.3}Ga_{0.7}As$ layers.

transparency carrier density begins to increase as the thicker QW allows more valence-band levels, which increase the density of valence states. To sum up, the finally optimized InAlGaAs QW thickness is 6.8 nm with 12.5% indium and 14% aluminum.

3.2. Temperature dependence of threshold current

The lasing wavelength of VCSELs is generally not the same as the gain-peak wavelength (λ_g), as it is determined by the resonance frequency in the cavity (λ_c). The effective gain provided for lasing is the gain where the cavity mode crosses with the gain spectrum.

Gain spectra of 6.8 nm $In_{0.125}Al_{0.14}Ga_{0.735}As$ QWs at different temperatures are plotted in figure 6(a) as solid lines with different colors. We estimate the cavity-mode wavelength by $\lambda_c = 794.7\ \text{nm} + 0.062\ \text{nm K}^{-1}\ (T - 358\ \text{K})$. This way, the gain-resonance cross value (we call it the cavity-mode gain, g_{cavity}) at different temperatures can be obtained and is indicated with red squares. Figure 6(b) shows g_{cavity} as a function of temperature extracted from figure 6(a). As can be seen, g_{cavity} is temperature dependent due to the different shift rates of λ_g and λ_c with the temperature. g_{cavity} reaches the maximum at about 340 K.

Since the required modal gain of the VCSEL is constant at threshold, the lower g_{cavity} requires higher current to maintain the threshold condition. Therefore, it is $g_{\text{cavity}}(T)$ in figure 6(b) that dominates the temperature dependence of the threshold current. Generally, the minimum threshold current (I_{min}) is thought to occur at the temperature T_{alig} at which the cavity resonance is spectrally aligned with the maximum gain in VCSELs [12]. However, for the designed VCSELs operating at 358 K, the gain decreases severely with the temperature rise and the temperature corresponding to I_{min} is lower than T_{alig}, as shown in figure 6(b). That is to say, although the cavity mode matches with the gain peak at T_{alig}, the corresponding gain is not highest. These results agree with the significant experiments on power saturation of 0.8 μm VCSELs [28, 29].

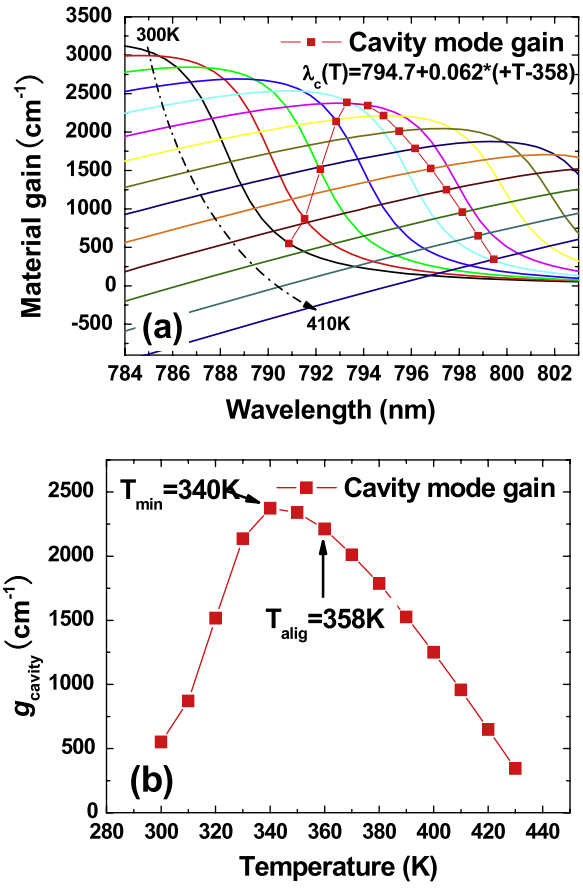

Figure 6. (a) Gain spectra of 6.8 nm $In_{0.125}Al_{0.14}Ga_{0.735}As/Al_{0.3}Ga_{0.7}As$ QWs at a constant carrier density (5×10^{18} cm^{-3}) for different temperatures. The solid box indicates the overlap of gain and cavity mode with increasing temperature. (b) Material gain at the cavity resonance (g_{cavity}) versus temperature for a constant current density (5×10^{18} cm^{-3}) extracted from (a).

3.3. Temperature dependence of light–current–voltage characteristics

The temperature distribution and temperature-dependent output of the proposed structure are studied and plotted in figures 7 and 8. The 2D contour plot of temperature distribution is from simulation of a VCSEL with 3 μm aperture and driven by 2 mA current at 358 K (only showing the area in the dashed panel in figure 1). It is observed that the highest temperature appears in the active region and the lowest temperature in the substrate. From the gradients of the temperature profile, it can be seen that the generated thermal energy dissipated effectively through the *n*-DBR and substrate. The temperature difference of the active region and substrate is 18 K at an ambient temperature of 358 K. The temperature difference is crucial for gain-offset design of VCSELs to get precise wavelength and low threshold current at elevated temperatures.

Figure 8 plots simulated *P–I–V* characteristics of VCSELs with 3 μm aperture at 300, 330 and 358 K. It is clearly shown that the proposed VCSEL keeps lasing at 358 K with threshold current of 0.9 mA and output more than 1 mW corresponding to a temperature of 376 K in the active region

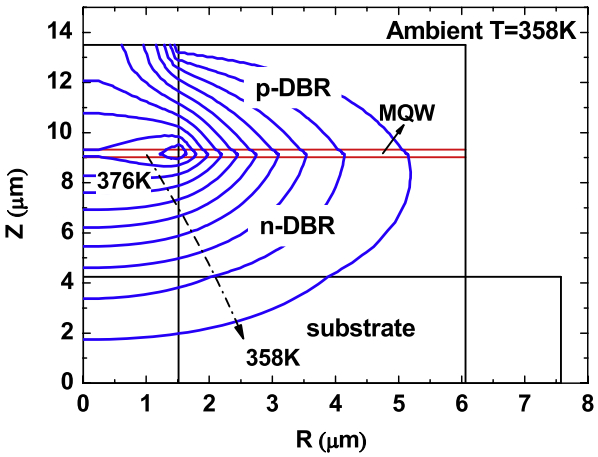

Figure 7. Contour plot of temperature distribution for the device with 3 μm aperture driven by 2 mA current at 358 K.

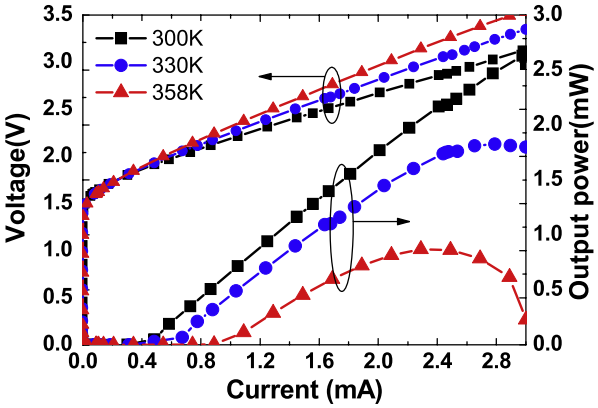

Figure 8. *P–I–V* characteristics of VCSELs with 3 μm aperture at different temperatures.

(see figure 7). The performance degenerates with the ambient temperature increasing from 300 to 358 K, which is reflected in the threshold current increase and slope efficiency decrease. These effects are mainly caused by the cavity-mode gain decreasing, as plotted in figure 6.

3.4. Temperature dependence of modulation response

In order to create FM sidebands, VCSELs for ^{87}Rb based CSACs must be modulated at 3.4 GHz (half the ground-state splitting frequency of ^{87}Rb) and therefore should have an FM modulation bandwidth above 3.4 GHz [16].

Modulation responses of the proposed 3 μm VCSEL at different currents at 345 K are depicted in figure 9(a). It is shown that increasing the injecting current shifts the response peaks to appear at higher frequencies while the magnitudes of the peaks decrease. The maximum 3 dB bandwidth at large current is limited by the superlinear increase of damping with resonance frequency and therefore excessive damping at high currents. However, a 3 dB bandwidth of 6 GHz is obtained at only 1.2 mA, which benefits from the high optical gain of the optimized compressively strained QWs.

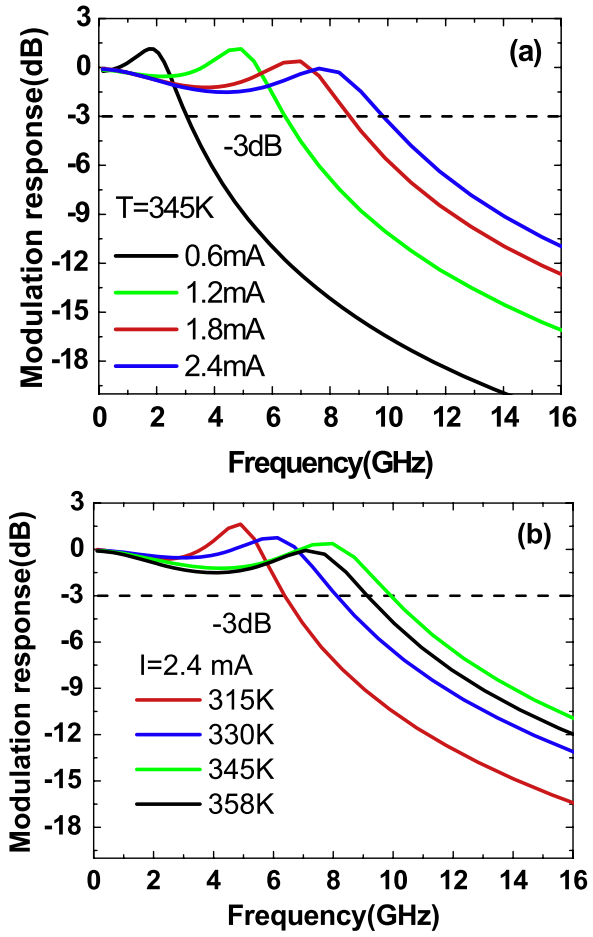

Figure 9. Modulation response of 795 nm VCSEL with 3 μm aperture under different currents (a) and elevated temperatures (b).

In order to study thermal effects on modulation responses, the bias current is fixed at 2.4 mA while the temperature varies from 315 to 358 K (see figure 9(b)). It is shown that the resonance frequency increases initially and reduces afterward with the increase of temperature. This is in accord with the general viewpoint that resonance frequency is proportional to the square root of the optical power. The maximum bandwidth of 10 GHz is obtained at 345 K, which well exceeds the 3.4 GHz specification for ^{87}Rb based CSACs.

4. Conclusion

We design and analyze the temperature sensitivity of high-temperature operating 795 nm VCSELs for atomic clocks. The InAlGaAs/AlGaAs QWs with variant compositions and thicknesses at different temperatures are theoretically optimized. The 6.8 nm thick InAlGaAs MQWs with 12.5% indium and 14% aluminum compositions are found to promise both low transparency carrier density and high material gain. The temperature sensitivity of the threshold current is analyzed by cavity-mode gain over a broad temperature range (300–430 K). The numerical results suggest that the minimum threshold current is found at a temperature lower than that when the cavity mode aligns the gain-peak wavelength. Based

on a self-consistent VCSEL model, a threshold current of 0.9 mA, output more than 1 mW and 3 dB bandwidth of 6 GHz are obtained from a 3 μm aperture 795 nm VCSEL at high temperatures.

Acknowledgments

This work is supported by the National Natural Science Foundation of China (NNSFC) under grant nos 61106047 and 51172225.

References

[1] Yang G, MacDougal M and Dapkus P 1995 *Electron. Lett.* **31** 886–8
[2] Alias M, Shaari S and Mitani S 2010 *Laser Phys.* **20** 806–10
[3] Chang Y C and Coldren L A 2009 *IEEE J. Sel. Top. Quantum Electron.* **15** 704–15
[4] Liu A, Chen W, Qu H, Jiang B, Zhou W, Xing M and Zheng W 2010 *Laser Phys. Lett.* **7** 213–7
[5] Wang Z, Ning Y, Zhang Y, Shi J, Zhang X, Zhang L, Wang W, Liu D, Hu Y and Cong H 2010 *Opt. Express* **18** 23900–5
[6] Serkland D, Geib K, Peake G, Lutwak R, Rashed A, Varghese M, Tepolt G and Prouty M 2007 *Proc. SPIE* **6484** 648406
[7] Arimondo E 1996 *Prog. Opt.* **35** 257–354
[8] Lutwak R, Deng J, Riley W, Varghese M, Leblanc J, Tepolt G, Mescher M, Serkland D, Geib K and Peake G 2004 *36th Annual Precise Time and Time Interval (PTTI) Meeting* p 339
[9] Tell B, Brown-Goebler K, Leibenguth R, Baez F and Lee Y 1992 *Appl. Phys. Lett.* **60** 683–5
[10] Baveja P P, Kogel B, Westbergh P, Gustavsson J S, Haglund A, Maywar D N, Agrawal G P and Larsson A 2012 *IEEE J. Quantum Electron.* **48** 17–26
[11] Herrick R W 2002 *Proc. SPIE* **4649** 130
[12] Mogg S, Chitica N, Christiansson U, Schatz R, Sundgren P, Asplund C and Hammar M 2004 *IEEE J. Quantum Electron.* **40** 453–62
[13] Chen C, Leisher P O, Allerman A A, Geib K M and Choquette K D 2006 *IEEE J. Quantum Electron.* **42** 1078–83
[14] Andre P, Antunes P, Teixeira A and Pinto J 2005 *Laser Phys. Lett.* **2** 525–8
[15] Derebezov I, Haisler V, Bakarov A, Kalagin A, Toropov A, Kachanova M, Gavrilova T, Semenova O, Tretyakov D and Beterov I 2010 *Semiconductors* **44** 1422–6
[16] Long C M and Choquette K D 2008 *J. Appl. Phys.* **103** 033101
[17] Van de Walle C 1989 *Phys. Rev.* B **39** 1871–83
[18] Chang Y A, Chen J R, Kuo H C, Kuo Y K and Wang S C 2006 *J. Light. Technol.* **24** 536
[19] Chuang S 1991 *Phys. Rev.* B **43** 9649–61
[20] Chuang S L 1995 *Physics of Optoelectronic Devices* (New York: Wiley)
[21] Passaro V, Magno F and De Leonardis F 2005 *Laser Phys. Lett.* **2** 239–46
[22] Piprek J 2003 *Semiconductor Optoelectronic Devices: Introduction to Physics and Simulation* (New York: Academic)
[23] Tromborg B, Lassen H, Olesen H and Pan X 1992 *IEEE Photon. Technol. Lett.* **4** 985–8
[24] Tromborg H O B and Pan X 1991 *IEEE J. Quantum Electron.* **27** 178–92
[25] Gao W, Xu Z, Cheng L, Luo K, Mastrovito A and Shen K 2008 *Proc. SPIE* **6456** 64560B-1
[26] Healy S B, O'Reilly E P, Gustavsson J S, Westbergh P, Haglund A, Larsson A and Joel A 2010 *IEEE J. Quantum Electron.* **46** 506–12
[27] Zhang Y, Ning Y, Zhang L, Zhang J, Wang Z, Zeng Y and Wang L 2011 *Opt. Express* **19** 12569–81
[28] Summers H, Wu J and Roberts J 2001 *IEE Proc. Optoelectron.* **148** 261–5
[29] Wu J, Xiao W and Lu Y M 2007 *IET Optoelectron.* **1** 206–10